

An adaptive virtual element method for the polymer self-consistent field theory

Huayi Wei, Xin Wang, Chunyu Chen, Kai Jiang*

School of Mathematics and Computational Science, Hunan Key Laboratory for Computation and Simulation in Science and Engineering, Xiangtan University, Xiangtan, Hunan, P.R. China, 411105.

Abstract

In this paper, we develop a high-order adaptive virtual element method (VEM) to simulate the self-consistent field theory (SCFT) model in arbitrary domains. The VEM is very flexible in handling general polygon elements and can treat hanging nodes as polygon vertices without additional processing. Besides, to effectively simulate the phase separation behavior in strong segregation systems, an adaptive method on polygonal mesh equipped with a new marking strategy is developed. This new marking strategy will indicate the times of marked elements to be refined and coarsened, making full use of the information contained in the current numerical results. Using the halfedge data structure, we can apply the adaptive method to the arbitrary polygonal mesh. Numerical results demonstrate that the developed method is efficient in simulating polymers' phase behavior in complex geometric domains. The accuracy is consistent with theoretical results. The adaptive method can greatly reduce computational costs to obtain prescribed numerical accuracy for strong segregation systems.

1. Introduction

Block polymers have attracted considerable attention for many years due to their industrial applications relying on customized microstructures. There are many industrial applications for the block-copolymer ordered structures at the nanoscale, such as the construction of high-capacity data storage devices, waveguides, quantum dot arrays, dielectric mirrors, nanoporous membranes, nanowires, and interference lithography [1, 2]. In the practical environment, geometric restriction strongly influences the formation of microstructures, which also provides a new opportunity to engineer novel structures. Concretely speaking, the confining geometries and surface interactions can result in structural frustration, confinement-induced entropy loss, and lead to novel morphologies that are not obtained in bulk systems [3, 4, 5].

Modeling and numerical simulation provide a practical means to investigate the phase separation behavior of polymer systems. Fully atomistic and coarse-graining approaches are both computational intensive methods for calculating equilibrium microstructures of polymer systems, especially for larger and more complicated geometries [6, 7]. A more and effective continuum approach is the self-consistent field theory (SCFT), which is one of the most successful modern tools for studying the phase behaviors of inhomogeneous polymer systems, such as self-assembly and thermodynamic stability. SCFT can efficiently describe polymer architecture, molecular composition, polydispersity, polymer subchain types, interaction potential, and related information as a series of parameters. SCFT modeling is started with a coarse-grained chain and microscopic interaction potentials used in the particle model, then transforms the particle-based model into a field-theoretic framework, finally derives a mean-field equations system within saddle-point approximation [8].

From the viewpoint of mathematics, the SCFT model is a complicated variational problem with many challenges, such as saddle-point, nonlinearity, multi-solutions and multi-parameters. It is not easy to obtain an analytical solution for this model. A numerical simulation is a feasible tool to solve SCFT, which usually consists of four parts: screening initial values [9, 10, 11], solving time-dependent partial differential equations (PDEs) [12, 13], evaluating (monomer) density operators [13], and finding

*Corresponding author. Email: kaijiang@xtu.edu.cn.

saddle-points [14, 15, 16]. The equilibrium state solution of the SCFT corresponds to an ordered microstructure. Due to the subtle energy difference among different ordered patterns in polymer systems, a high order numerical method is strongly needed.

In the past several decades, spectral methods, especially the Fourier spectral method, have been the predominant tool for solving the SCFT model [17, 18, 19]. This approach has high-order precision and is efficient when a spectral collocation method is found. However, the spectral method uses the global basis functions to discretize the spatial functions, limiting its applications on the model defined on complex geometric domains and complex boundary conditions. An alternative approach uses local basis functions to discretize spatial functions, such as the finite element method (FEM) [20, 21]. The FEM precision depends on the size and quality of the mesh and the order of local polynomial basis functions. Combined with the adaptive method [22], FEM can obtain a more accurate numerical solution with less calculation cost. However, there is some inconvenience when using the FEM with the adaptive method, especially when the adaptive mesh contains hanging nodes [23], polygonal, or concave mesh elements.

To address these problems, in this work, we develop an efficient approach to solve the SCFT model in general domains based on the virtual element method (VEM). The VEM can be considered as an extension of conforming FEM to polygonal meshes, which has been developed to solve a variety of PDEs, see [24, 25, 26, 27, 28, 29] and references therein. This paper's contribution contains: (a) formulating the SCFT problem in real space using a high-order VEM-based variational form, (b) proposing a new adaptive approach that can make full use of obtained numerical results, (c) using a halfedge data structure to refine and coarsen general polygonal grids, (d) the capacity of computing highly segregated systems in arbitrary areas with the economical computational amount.

The remaining sections are organized as follows. In Sec. 2, we give the SCFT model defined in the general domain using the Gaussian diblock chains as an example. In Sec. 3, we present the high-order adaptive VEM to solve SCFT in detail. In Sec. 4, we demonstrate the precision and efficiency of our methods by plenty of numerical experiments. In Sec. 5, we end with several concluding remarks and future work.

2. Self-consistent field theory

In this section, we give a brief introduction to the SCFT model for an incompressible AB diblock copolymer melt on an arbitrary domain Ω . We consider a system with n conformationally symmetric diblock copolymers and each has A and B arms joined together with a covalent bond. The total degree of polymerization of a diblock copolymer is N , the A-monomer fraction is f , and the B-monomer fraction is $1 - f$. The field-based Hamiltonian within mean-field approximation for the incompressible diblock copolymer melt is [8, 19]

$$H = \frac{1}{|\Omega|} \int_{\Omega} \left\{ -w_+(\mathbf{r}) + \frac{w_-^2(\mathbf{r})}{\chi N} \right\} d\mathbf{r} - \log Q[w_+(\mathbf{r}), w_-(\mathbf{r})], \quad (1)$$

where χ is the Flory-Huggins parameter to describe the interaction between segments A and B. The terms $w_+(\mathbf{r})$ and $w_-(\mathbf{r})$ can be viewed as fluctuating pressure and exchange chemical potential fields, respectively. The pressure field enforces the local incompressibility, while the exchange chemical potential is conjugate to the difference of density operators. Q is the single chain partition function, which can be computed according to

$$Q = \frac{1}{|\Omega|} \int_{\Omega} q(\mathbf{r}, s) q^\dagger(\mathbf{r}, s) d\mathbf{r}, \quad \forall s \in [0, 1].$$

The forward propagator $q(\mathbf{r}, s)$ represents the probability weight that the chain of contour length s has its end at position \mathbf{r} . The variable s is used to parameterize each copolymer chain such that $s = 0$ represents the tail of the A block and $s = f$ is the junction between the A and B blocks. According to the flexible Gaussian chain model [8], $q(\mathbf{r}, s)$ satisfies the following PDE

$$\begin{aligned} \frac{\partial}{\partial s} q(\mathbf{r}, s) &= R_g^2 \nabla_{\mathbf{r}}^2 q(\mathbf{r}, s) - w(\mathbf{r}, s) q(\mathbf{r}, s), \quad \mathbf{r} \in \Omega, \\ w(\mathbf{r}, s) &= \begin{cases} w_A(\mathbf{r}) = w_+(\mathbf{r}) - w_-(\mathbf{r}), & 0 \leq s \leq f, \\ w_B(\mathbf{r}) = w_+(\mathbf{r}) + w_-(\mathbf{r}), & f \leq s \leq 1, \end{cases} \end{aligned} \quad (2a)$$

with the initial condition $q(\mathbf{r}, 0) = 1$ and R_g being the radius of gyration. The above PDE is well-defined by possessing an appropriate boundary condition. In this work, we consider the homogeneous Neumann boundary condition

$$\frac{\partial}{\partial \mathbf{n}} q(\mathbf{r}, s) = 0, \quad \mathbf{r} \in \partial\Omega.$$

The backward propagator $q^\dagger(\mathbf{r}, s)$, which represents the probability weight from $s = 1$ to $s = 0$, satisfies Eqn. (2) only with the right-hand side of Eqn.(2a) multiplied by -1 . The initial condition is $q^\dagger(\mathbf{r}, 1) = 1$. The normalized segment density operators $\phi_A(\mathbf{r})$ and $\phi_B(\mathbf{r})$ follow from functional derivatives of Q with respect to w_A and w_B and the familiar factorization property of propagators

$$\phi_A(\mathbf{r}) = -\frac{V}{Q} \frac{\delta Q}{\delta w_A} = \frac{1}{Q} \int_0^f q(\mathbf{r}, s) q^\dagger(\mathbf{r}, s) ds, \quad (3)$$

$$\phi_B(\mathbf{r}) = -\frac{V}{Q} \frac{\delta Q}{\delta w_B} = \frac{1}{Q} \int_f^1 q(\mathbf{r}, s) q^\dagger(\mathbf{r}, s) ds. \quad (4)$$

The first-order variations of the Hamiltonian with respect to fields w_+ and w_- lead to the mean-field equations

$$\begin{aligned} \frac{\delta H}{\delta w_+} &= \phi_A(\mathbf{r}) + \phi_B(\mathbf{r}) - 1 = 0, \\ \frac{\delta H}{\delta w_-} &= \frac{2w_-(\mathbf{r})}{\chi N} - [\phi_A(\mathbf{r}) - \phi_B(\mathbf{r})] = 0. \end{aligned}$$

The equilibrium state, i.e., $\delta H / \delta w_\pm = 0$, of the SCFT model corresponds to the ordered structure. Within the standard framework of SCFT, finding the stationary states requires the self-consistent iterative procedure, as shown in the following flowchart.

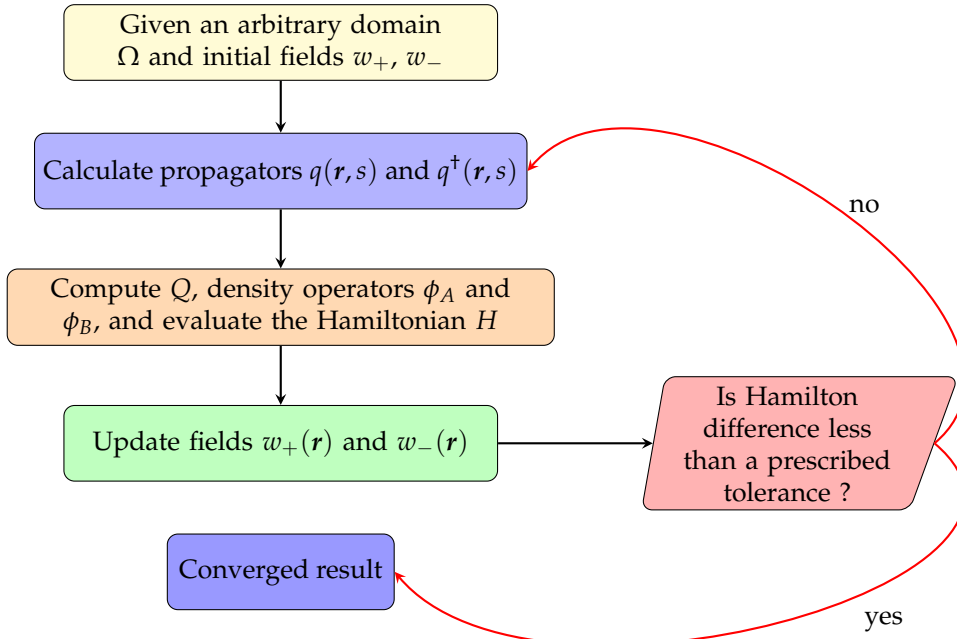


Figure 1: Flowchart of SCFT iteration.

The propagator equation is dependent on the potential fields $w_+(\mathbf{r})$ and $w_-(\mathbf{r})$. In order to start the process, the values of $w_+(\mathbf{r})$ and $w_-(\mathbf{r})$ must be initialized. If the initial values are homogeneous, the gradient term in the modified diffusion equation goes to zero, leaving no driving force for forming a microstructure. To prevent this, there must be some spatial inhomogeneity in the initial values. For a targeted periodic structure, using the space group symmetry is a useful strategy to screen the initial

configuration [10, 11]. Once initial values are ready, high-accuracy numerical methods to solve the propagator equation, and evaluate the density functions, are required to solve the SCFT model, which is also the main work in this paper. We will detail our approach in Sec. 3.

The iteration method to update fields is dependent on the mathematical structure of SCFT. An important fact is that the effective Hamiltonian (1) of diblock copolymers can reach its local minima along the exchange chemical field $w_-(\mathbf{r})$, and achieve the maxima along the pressure field $w_+(\mathbf{r})$ [8]. Thus alternative direction gradient approaches, such as the explicit Euler method, can be used to find the saddle point. In particular, the explicit Euler approach is expressed as

$$\begin{aligned} w_+^{k+1}(\mathbf{r}) &= w_+^k(\mathbf{r}) + \lambda_+ \left(\phi_A^k(\mathbf{r}) + \phi_B^k(\mathbf{r}) - 1 \right), \\ w_-^{k+1}(\mathbf{r}) &= w_-^k(\mathbf{r}) - \lambda_- \left(\frac{2w_-^k(\mathbf{r})}{\chi N} - [\phi_A(\mathbf{r}) - \phi_B(\mathbf{r})] \right). \end{aligned}$$

An accelerated semi-implicit scheme has been developed to find the equilibrium states [14, 16]. However, the existing semi-implicit method is based on the asymptotic expansion and global Fourier transformation and can not be straightforwardly applied to the local basis discretization schemes.

3. Numerical methods

Solving the propagator equations is the most time-consuming part of the entire numerical simulation, and we will discuss its spatial variables discretization with the (adaptive) VEM in detail in this section. In the following, we use the $\|\cdot\|_B$ to denote the common L^2 norm over a finite domain B .

3.1. VEM discretization for the spatial variable

VEM is a generalization of the finite element method inspired by the modern mimetic finite difference scheme [25]. Compared with FEM, VEM can handle general (even non-convex) polygonal elements. Furthermore, VEM can naturally treat the hanging nodes appearing in the mesh adaptive process as the vertices of the polygonal elements, which greatly simplifies the design and implementation of mesh adaptive algorithms. Fig. 2 gives a schematic mesh which the VEM can deal with. Subse-

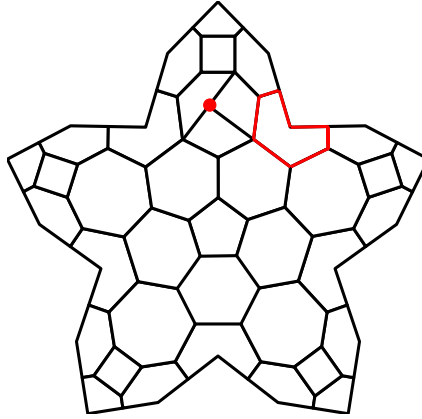


Figure 2: A schematic mesh of the VEM including hanging node and concave polygons.

quently, we will introduce the virtual element space and discretize propagator equations (2) based on the variational formulation.

3.1.1. Virtual element space

Let Ω_h be the polygonal decomposition of a given domain $\Omega \subset \mathbb{R}^2$ including a finite number of non-overlapping polygons. For any polygonal element $E \in \Omega_h$, let $\partial E = \{e\}$ be the set of all boundary edges of E , \mathbf{r}_E the barycenter, h_E the diameter, and $|E|$ the area of the element E . Let $\mathcal{P}_k(E)$ be the polynomials space of degree up to k on E , $n_k = \dim \mathcal{P}_k(E) = (n_k + 1)(n_k + 2)/2$, and $\mathcal{M}_k(E) := \{m_\alpha : 0 \leq |\alpha| \leq k\}$ be the scaled monomial basis set of $\mathcal{P}_k(E)$ with form [26]

$$m_\alpha := \left(\frac{\mathbf{r} - \mathbf{r}_E}{h_E} \right)^\alpha = \frac{(r_1 - r_{1E})^{\alpha_1} (r_2 - r_{2E})^{\alpha_2}}{h_E^{\alpha_1 + \alpha_2}}, \quad \alpha_1, \alpha_2 \in \mathbb{Z}_0^+,$$

and $|\alpha| = \alpha_1 + \alpha_2$. We will use m_α instead of m_α , where α is a one-dimensional index of the natural correspondence of α , for example,

$$(0,0) \leftrightarrow 1, (1,0) \leftrightarrow 2, (0,1) \leftrightarrow 3, (2,0) \leftrightarrow 4, \dots$$

The local virtual element space can be defined as [24, 26]

$$V_{h,E} := \{v \in H^1(E) : \Delta v \in \mathcal{P}_{k-2}(E) \text{ in } E; v|_e \in \mathcal{P}_k(e), \forall e \in \partial E\},$$

where Δ denotes the common Laplace operator. $\mathcal{P}_k(e)$ is a set of polynomials of degree up to k on e . The dimension of $V_{h,E}$ is

$$N_{dof} = \dim V_{h,E} = n_V + n_V(k-1) + n_{k-2}$$

where n_V is the number of vertices of E . The function $v_h \in V_{h,E}$ can be defined by satisfying the following three conditions:

- $v_h|_e \in \mathcal{P}_k(e)$ is a polynomial of degree k on each edge e ;
- $v_h|_{\partial E} \in C(\partial E)$ is globally continuous on ∂E ;
- $\Delta v_h \in \mathcal{P}_{k-2}(E)$ is a polynomial of degree $k-2$ in E .

Correspondingly, the degree of freedom of the $V_{h,E}$ contains:

- the value of v_h at the vertices of E ;
- the value of v_h at the $k-1$ internal Gauss-Lobatto quadrature points on e ;
- the moments up to order $k-2$ of v_h in E : $\frac{1}{E} \int_E v_h m_\alpha d\mathbf{r}, \alpha = 1, \dots, n_k$.

Then the global virtual element space can be defined based on the local space $V_{h,E}$,

$$V_h = \{v \in H^1(E) : v|_E \in V_{h,E}, \text{ for all } E \in \Omega_h\}.$$

The dimension of V_h is

$$N = \dim V_h = N_V + N_E(k-1) + N_P n_{k-2},$$

where N_V , N_E and N_P are the total number of vertices, edges, and elements of Ω_h , respectively. Since $H^1(V_h)$ is a separable Hilbert space, it can give a set of basis functions $\{\varphi_i(\mathbf{r})\}_{i=1}^N$ for V_h such that, for each $u_h(\mathbf{r}) \in V_h$

$$u_h(\mathbf{r}) = \sum_{i=1}^N u_i \varphi_i(\mathbf{r}), \quad (5)$$

where u_i is the coefficient of the degree of freedom corresponding to $\varphi_i(\mathbf{r})$. It should be emphasized that the basis functions $\varphi_i(\mathbf{r})$ in the VEM do not have explicit expression as the FEM has. In practical implementation, the quantities related to the basis functions can be obtained through the degree of freedom.

3.1.2. Variational formulation

Using VEM to solve PDEs (2) is based on the variational formulation whose continuous version is: find $q(\mathbf{r}, s) \in H^1(\Omega)$ such that, for all $v(\mathbf{r}) \in H^1(\Omega)$,

$$\left(\frac{\partial}{\partial s} q(\mathbf{r}, s), v(\mathbf{r}) \right) = -(\nabla q(\mathbf{r}, s), \nabla v(\mathbf{r})) - (w(\mathbf{r}, s)q(\mathbf{r}, s), v(\mathbf{r})), \quad (6)$$

where (\cdot, \cdot) represents the $L^2(\Omega)$ inner product. In numerical computation, the spatial function must be discretized in the finite-dimensional virtual element space V_h . Then the continuous variational formulation (6) is discretized as: find $q_h(\mathbf{r}, s) \in V_h$ such that

$$\left(\frac{\partial}{\partial s} q_h(\mathbf{r}, s), v_h(\mathbf{r}) \right) = -(\nabla q_h(\mathbf{r}, s), \nabla v_h(\mathbf{r})) - (w(\mathbf{r}, s)q_h(\mathbf{r}, s), v_h(\mathbf{r})), \text{ for all } v_h(\mathbf{r}) \in V_h. \quad (7)$$

Let $v_h(\mathbf{r}) = \varphi_j(\mathbf{r})$, using the expression (5), $q_h(\mathbf{r}, s) = \sum_{i=1}^N q_i(s) \varphi_i(\mathbf{r})$. The discretized variational formulation (7) has the matrix form

$$\mathbf{M} \frac{\partial}{\partial s} \mathbf{q}(s) = -(\mathbf{A} + \mathbf{F}) \mathbf{q}(s), \quad (8)$$

where

$$\mathbf{q}(s) = (q_1(s), q_2(s), \dots, q_N(s))^T,$$

and

$$\mathbf{M}_{ij} = (\varphi_i, \varphi_j), \quad \mathbf{A}_{ij} = (\nabla \varphi_i, \nabla \varphi_j), \quad \mathbf{F}_{ij} = (w(\mathbf{r}, s) \varphi_i, \varphi_j), \quad i, j = 1, \dots, N.$$

The stiffness matrix \mathbf{A} , the mass matrix \mathbf{M} , and the cross mass matrix \mathbf{F} can be obtained through projecting local virtual element space $V_{h,E}$ onto polynomial space. In the sequential subsections, we will present the construction methods for local stiffness, mass, and cross mass matrices. The corresponding global matrices \mathbf{A} , \mathbf{M} and \mathbf{F} can be obtained as the standard assembly process of FEM once we have the local ones.

3.1.3. Stiffness matrix

The stiffness matrix in the VEM can be computed by the local H^1 projection operator Π^∇ ,

$$\Pi^\nabla : V_{h,E} \rightarrow \mathcal{P}_k(E),$$

which projects the local virtual element space $V_{h,E}$ onto the polynomial space with degree up to k . For each $v_h \in V_{h,E}$, we have the orthogonality condition

$$(\nabla p, \nabla(\Pi^\nabla v_h - v_h)) = 0, \quad \text{for all } p \in \mathcal{P}_k(E).$$

The above condition defines $\Pi^\nabla v_h$ only up to a constant. It can be fixed by prescribing a projection operator onto constants P_0 requiring

$$P_0(\Pi^\nabla v_h - v_h) = 0.$$

P_0 can be chosen as

$$P_0 v_h := \frac{1}{n_V} \sum_{i=1}^{n_V} v_h(\mathbf{r}_i), \quad \text{when } k = 1,$$

$$P_0 v_h := \frac{1}{|E|} \int_E v_h \, d\mathbf{r} = \frac{1}{|E|} (1, v_h)_E, \quad \text{when } k \geq 2,$$

where n_V is the number of vertices of E .

Next we compute the local stiffness matrix $(\mathbf{A}^E)_{ij}$ on the polygon E ,

$$(\mathbf{A}^E)_{ij} = (\nabla \varphi_i, \nabla \varphi_j), \quad i, j = 1, \dots, N_{dof}. \quad (9)$$

With the operator Π^∇ , φ_i can be split into

$$\varphi_i = \Pi^\nabla \varphi_i + (\mathbf{I} - \Pi^\nabla) \varphi_i,$$

Eqn. (9) becomes

$$(\mathbf{A}^E)_{ij} = (\nabla \Pi^\nabla \varphi_i, \nabla \Pi^\nabla \varphi_j) + (\nabla (\mathbf{I} - \Pi^\nabla) \varphi_i, \nabla (\mathbf{I} - \Pi^\nabla) \varphi_j).$$

Replacing the second term as

$$S_0^E \left((\mathbf{I} - \Pi^\nabla) \varphi_i, (\mathbf{I} - \Pi^\nabla) \varphi_j \right) := \sum_{r=1}^{N_{dof}} \text{dof}_r \left((\mathbf{I} - \Pi^\nabla) \varphi_i \right) \text{dof}_r \left((\mathbf{I} - \Pi^\nabla) \varphi_j \right),$$

where $\text{dof}_r(\varphi_i) = \delta_{ri}$, we obtain the approximate local stiffness matrix

$$(\mathbf{A}_h^E)_{ij} := (\nabla \Pi^\nabla \varphi_i, \nabla \Pi^\nabla \varphi_j) + S_0^E \left((\mathbf{I} - \Pi^\nabla) \varphi_i, (\mathbf{I} - \Pi^\nabla) \varphi_j \right).$$

3.1.4. Mass matrix

The mass matrix in the VEM can be obtained from the local L^2 projection $\Pi : V_{h,E} \rightarrow \mathcal{P}_k(E)$. For each $v_h \in V_{h,E}$,

$$(\Pi v_h, p_k) = (v_h, p_k), \quad \forall p_k \in \mathcal{P}_k(E).$$

where (v_h, p_k) can not be calculated directly. Next, we show how to compute the local mass matrix \mathbf{M}^E [25]

$$(\mathbf{M}^E)_{ij} = (\varphi_i, \varphi_j), \quad i, j = 1, \dots, N_{dof}.$$

Similar to the construction method of the stiffness matrix, we define the basis function φ_i through L^2 projection operator Π

$$\varphi_i = \Pi \varphi_i + (\mathbf{I} - \Pi) \varphi_i.$$

Then

$$(\mathbf{M}^E)_{ij} = (\Pi \varphi_i, \Pi \varphi_j) + ((\mathbf{I} - \Pi) \varphi_i, (\mathbf{I} - \Pi) \varphi_j).$$

Replacing the second term in the above equation as

$$S_1^E ((\mathbf{I} - \Pi) \varphi_i, (\mathbf{I} - \Pi) \varphi_j) := |E| \sum_{r=1}^{N_{dof}} \text{dof}_r ((\mathbf{I} - \Pi) \varphi_i) \text{dof}_r ((\mathbf{I} - \Pi) \varphi_j)$$

the local mass matrix is approximated as

$$(\mathbf{M}_h^E)_{ij} := (\Pi \varphi_i, \Pi \varphi_j) + S_1^E ((\mathbf{I} - \Pi) \varphi_i, (\mathbf{I} - \Pi) \varphi_j)$$

3.1.5. Cross mass matrix

The local cross mass matrix \mathbf{F}_{ij} on E can be defined as

$$(\mathbf{F}_E)_{ij} = (w \varphi_i, \varphi_j), \quad i, j = 1, \dots, N_{dof}.$$

Applying the L^2 projection $\Pi : V_{h,E} \rightarrow \mathcal{P}_k(E)$, as defined in the above Sec. 3.1.4, into the cross term, the local mass matrix can be calculated as

$$(\mathbf{F}_E)_{ij} := (\Pi w \Pi \varphi_i, \Pi \varphi_j).$$

3.1.6. Spatial integral

Here we present the integration approach over an arbitrary polygon E . We divide the polygon E into triangles τ by linking two endpoints of each edge and the barycenter. Then we apply the common Gaussian quadrature in each triangle, and summarize these integration values.

$$\int_E f(\mathbf{r}) d\mathbf{r} = \sum_{\tau} \int_{\tau} f(\mathbf{r}) d\mathbf{r} \approx |E| \sum_{\tau} \sum_j w_{\tau,j} f(\mathbf{r}_{\tau,j}),$$

where $\{\mathbf{r}_{\tau,j}\}$ is the set of quadrature points of τ , and $\{w_{\tau,j}\}$ the corresponding quadrature weights.

3.2. Adaptive technique

The adaptive method is an important technique to improve the solution's accuracy and reduce computational complexity. The following is the adaptive process used in SCFT calculation:

Step 1 Solve the SCFT model and obtain the numerical solution on the current mesh.

Step 2 Estimate error on each element from current numerical results.

Step 3 Mark mesh elements according to the error estimate.

Step 4 Refine or coarsen the marked elements.

Next, we present some implementation details of the above adaptive process.

The estimator is an important part of the adaptive method. Let η_E be the error of the indicator function u_h over each element E ,

$$\eta_E = \|R_h \Pi^\nabla u_h\|_E, \quad (10)$$

$R_h u_h$ is the harmonic average operator [30]

$$R_h u_h := \frac{1}{\sum_{j=1}^{m_z} 1/|\tau_j|} \sum_{j=1}^{m_z} \frac{1}{|\tau_j|} \nabla \Pi^\nabla u_h \Big|_{\tau_j}.$$

m_z is the number of elements τ_j with z as a vertex. The indicator function is an essential part of adaptive methods. In the SCFT model, several spatial functions can be used as indicator functions, such as field functions, density functions, and propagators. To choose an efficient indicator function, we observe the distribution of these spatial functions when the SCFT calculation converges. As an example, Fig. 3 presents the equilibrium states of $w(\mathbf{r})$, $\varphi_A(\mathbf{r})$ and propagator function of the last contour point $q(\mathbf{r}, 1)$, respectively, with $\chi N = 25, f = 0.2$. As one can see, the distributions of three spatial functions are similar, however, $q(\mathbf{r}, 1)$ has the sharpest interface. If the numerical error of $q(\mathbf{r}, 1)$ can be reduced through the adaptive method, the error of other spatial functions obviously reduces with it. Therefore, in the current adaptive method, we choose $q(\mathbf{r}, 1)$ as the indicator function in the posterior error estimator.

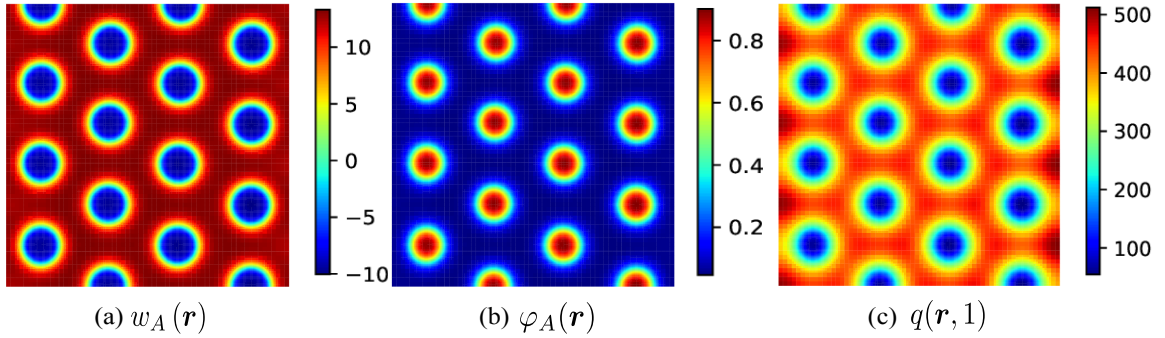


Figure 3: The equilibrium distributions of $w_A(\mathbf{r})$, $\varphi_A(\mathbf{r})$, and $q(\mathbf{r}, 1)$ when $\chi N = 25, f = 0.2$.

Given an effective and reliable posterior error estimator η_E , a marking strategy is required to mark mesh elements. Classical marking strategies such as the maximum [31] and the L^2 criterion [32], usually refine or coarsen marked mesh elements one time in one adaptive process. It may make less use of the information of the posterior error estimator. To improve it, we propose a new marking strategy, named *Log* criterion, as following

$$n_E = \left[\log_2 \frac{\eta_E}{\theta \bar{\eta}} \right],$$

where θ is a positive constant, $\bar{\eta}$ is the mean value of all element estimator η_E , and $[\cdot]$ is the nearest integer function. $n_E = 0, n_E > 0$ and $n_E < 0$ represent that cell E is unchanged, refined n_E times, and coarsened $|n_E|$ times, respectively. Obviously, this new *Log* marking criterion not only denotes which mesh element E needs to be improved but also provides the times of refinement or coarseness.

We use the halfedge data structure to implement our adaptive technique which allows us to refine and coarsen arbitrary polygonal mesh. Halfedge data structure is an edge-centered data structure capable of maintaining incidence information of nodes, edges, and cells [33]. Each edge is decomposed into two halfedges with opposite orientations. One incident cell and one incident node are stored in each halfedge. For each cell and each node, one incident halfedge is stored, see Fig. 4. Halfedge data structure is more flexible and powerful than the cell-centered data structure. The cell-centered data structure, as a classical data structure, stores the coordinates and indexes of each cell node and requires additional work to reconstruct the relationships between nodes, edges, and cells. Based on the halfedge data structure, the mesh adaptation is a process of increasing or decreasing the halfedges, as shown in Fig. 5. Notice that, based on the halfedge data structure, the current mesh refinement and coarsening algorithm, including the red-green approach [34], newest vertex bisection [35] and coarsening [36], can be implemented in a unified way. One can find the implementation in package FEALPy [37]

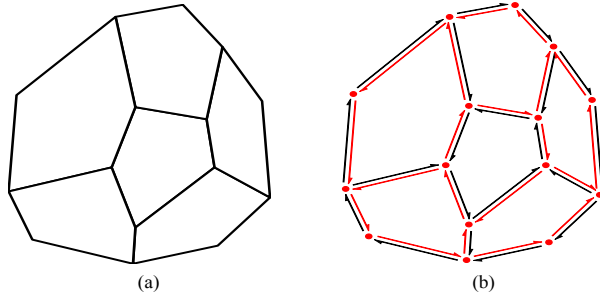


Figure 4: (a) A polygonal mesh. (b) The corresponding halfedge data structure of (a).

Once one has the adaptive mesh, the construction of stiffness, mass, cross mass matrices, and the spatial integral formula are the same as Secs. 3.1.3-3.1.6 present.

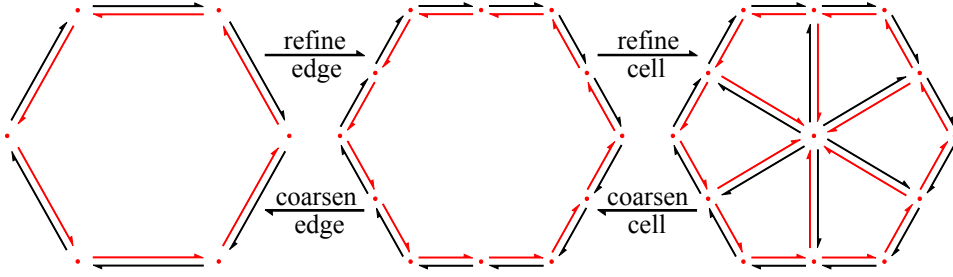


Figure 5: The refinement and coarsening of halfedge mesh.

3.3. Full-discrete form

The above matrix form (8) is still continuous in the contour variable s . There are numerous ways to discretize the contour, such as the second-order operator splitting method, the backward differentiation formulas, Crank-Nicolson (CN) scheme [18, 19, 21]. Recently, Cenicerros introduced the spectral deferred correction (SDC) approach to improve the accuracy and efficiency of solving polymer SCFT [13]. In the VEM framework, we choose the SDC scheme to discretize the contour variable. The SDC scheme stemmed from Dutt et al.'s work in 2000 [38], first solves the PDE with an appropriate method, then uses the residual equation to improve the approximation order of numerical solution. The key idea of SDC is to use spectral quadratures, such as a Gaussian or a Chebyshev-node interpolatory quadrature, to integrate the contour derivative, which can achieve a high-accuracy numerical solution with a vastly reduced number of quadrature points. The detail will be presented in sequential content.

We use the variable step Crank-Nicolson (CN) scheme to solve the semi-discrete propagator equation (8) and obtain the initial numerical solution $\mathbf{q}^{[0]}(s)$.

$$\mathbf{M} \frac{\mathbf{q}^{n+1} - \mathbf{q}^n}{\delta s_n} = -\frac{1}{2}(\mathbf{A} + \mathbf{F})(\mathbf{q}^{n+1} + \mathbf{q}^n), \quad (11)$$

where $\delta s_n = s_{n+1} - s_n$ is the time step size, s_n ($n = 0, 1, \dots, N_s - 1$) is the Chebyshev node [39]. It should be pointed out that other stable time schemes can be employed to solve semi-discrete propagator equation (8), such as the second-order operator-splitting method [18], implicit-explicit Runge-Kutta scheme [40, 13].

Then we use the deferred correction scheme to achieve a high-accuracy numerical solution. We can give the exact semi-discrete solution of propagator by integrating (8) along the contour variable s

$$\mathbf{M}\mathbf{q}(s) = \mathbf{M}\mathbf{q}(0) + \int_0^s [(-\mathbf{A} - \mathbf{F})\mathbf{q}(\tau)] d\tau.$$

The error between the numerical solution $\mathbf{q}^{[0]}(s)$ and the exact semi-discrete solution $\mathbf{q}(s)$ is defined as

$$\mathbf{e}^{[0]}(s) = \mathbf{q}(s) - \mathbf{q}^{[0]}(s).$$

Multiplying both sides by M , we have

$$\begin{aligned}
M\mathbf{e}^{[0]}(s) &= M\mathbf{q}(s) - M\mathbf{q}^{[0]}(s) \\
&= M\mathbf{q}(0) + \int_0^s [(-A - F)\mathbf{q}(\tau)] d\tau - M\mathbf{q}^{[0]}(s) \\
&= M\mathbf{q}(0) + \int_0^s [(-A - F)\mathbf{e}^{[0]}(\tau)] d\tau + \int_0^s [(-A - F)\mathbf{q}^{[0]}(\tau)] d\tau - M\mathbf{q}^{[0]}(\tau)(s) \\
&= \int_0^s [(-A - F)\mathbf{e}^{[0]}] d\tau + \gamma^{[0]}(s),
\end{aligned}$$

the residual

$$\gamma^{[0]}(s) = M\mathbf{q}(0) + \int_0^s [(-A - F)\mathbf{q}^{[0]}(\tau)] d\tau - M\mathbf{q}^{[0]}(s), \quad (12)$$

can be computed by the spectral integral method with Chebyshev-nodes as presented in the Appendix. By the definition of residual $\gamma^{[0]}$, we have the error integration equation

$$M\mathbf{e}^{[0]}(s) = \int_0^s (-A - F)\mathbf{e}^{[0]}(\tau) d\tau + \gamma^{[0]}(s).$$

Taking the first derivative of the above equation with respect to s leads to

$$M \frac{d\mathbf{e}^{[0]}}{ds} = (-A - F)\mathbf{e}^{[0]}(s) + \frac{d\gamma^{[0]}}{ds}, \quad (13)$$

which can also be solved by the variable step CN scheme (11). Then the corrected numerical solution is

$$\mathbf{q}^{[1]}(s) = \mathbf{q}^{[0]}(s) + \mathbf{e}^{[0]}(s).$$

Repeating the above process, one can have $\mathbf{q}^{[2]}, \dots, \mathbf{q}^{[J]}$, J is the pre-determined number of deferred corrections. The convergent order of deferred correction solution along the contour parameter is

$$\|\mathbf{q}(s) - \mathbf{q}^{[J]}(s)\| = O((\delta s)^{m(J+1)})$$

where $\delta s = \max\{\delta s_n\}_{n=0}^{N_s-1}$, m is the order of the chosen numerical scheme to solve Eqns. (8) and (13). For the CN scheme, $m = 2$.

In summary, under an appropriate regularity hypothesis [26, 38], one can prove the estimator for the numerical solution $q_{\delta s, h}$,

$$\|q_e - q_{\delta s, h}\| = O((\delta s)^{m(J+1)} + h^{k+1})$$

q_e is the true solution of propagator, and $h = \max_{E \in \Omega_h} \text{diam}\{E\}$.

4. Numerical results

In the following numerical examples, we use linear ($k = 1$) and quadratic ($k = 2$) VEMs to discretize the spatial variable. Due to the limitation of spatial discretization order, in the time direction, we correct the initial numerical solution one time in the SDC scheme. All the numerical examples are implemented based on the FEALPy package [37]. Halfedge data structure has also been integrated into FEALPy package.

4.1. VEM with uniform mesh

4.1.1. Solving a parabolic equation

Solving the PDE of parabolic type is the most time-consuming part of SCFT simulations. In this subsection, we examine the precision of our proposed method in solving a parabolic equation. We consider the following parabolic equation (14)

$$\begin{cases} \frac{\partial}{\partial s} u(x, y, s) = \frac{1}{2} \Delta u(x, y, s), & (x, y) \in \Omega = [0, 2\pi]^2, s \in [0, S], \\ \frac{\partial}{\partial \mathbf{n}} u(x, y, s) = 0, & (x, y) \in \partial\Omega, \\ u(x, y, 0) = \cos x \cos y, \end{cases} \quad (14)$$

with exact solution $u^e(x, y, s) = e^{-s} \cos x \cos y$.

First, we verify the convergent order of the linear and quadratic VEMs. The CN scheme with $\delta s = 1 \times 10^{-4}$ is used to guarantee enough time discretization accuracy. Tab. 1 gives the error and convergent order of VEM which is consistent with theoretical results.

Table 1: The error order of VEM.

Nodes	Linear VEM		Quadratic VEM	
	$\ u^e(\cdot, 1) - u_h(\cdot, 1)\ _\Omega$	order	$\ u^e(\cdot, 1) - u_h(\cdot, 1)\ _\Omega$	order
289	4.7737e-02	–	1.2062e-03	–
1089	1.3267e-02	1.84	1.5084e-04	2.99
4225	3.4013e-03	1.96	1.8863e-05	2.99
16641	8.5563e-04	1.99	2.3582e-06	3.00

Second, we verify the error order of the CN and SDC schemes for solving (14). For the SDC scheme, we obtain a new solution $u^{[1]}$ by correcting the initial numerical solution $u^{[0]}$ calculated by the CN scheme just once. For the spatial direction, we use the quadratic VEM with 66049 nodes to guarantee the spatial discretization accuracy. Tab. 2 gives the convergent order of the time discretization schemes which are also consistent with theoretical results. Note that the error showed above is the L^2 error between the true solution and numerical solution at $S = 1$.

Table 2: The error order of the time discretization schemes.

N_s	CN		SDC	
	$\ u^e(\cdot, s) - u_h(\cdot, s)\ _\Omega$	order	$\ u^e(\cdot, s) - u_h(\cdot, s)\ _\Omega$	order
4	6.0605e-03	–	5.7514e-04	–
8	1.5074e-03	2.00	1.0163e-05	5.82
16	3.7637e-04	2.00	6.4626e-07	3.97
32	9.4065e-05	2.00	4.2283e-08	3.94

Third, we verify the integral accuracy of the numerical solution along with the contour variable s which is required in solving PDEs and evaluating density functions. We use the quadratic VEM (66049 nodes) to discretize the parabolic equation (14) and obtain a semi-discrete matrix system. Correspondingly, the exact solution of (14) can be discretized into u_h^e . Then we solve the semi-discrete system using the CN and the SDC schemes for $s \in [0, 1]$ to obtain the numerical solutions u_h^{CN} and u_h^{SDC} , respectively. We integrate u_h^{CN} and u_h^{SDC} along s from 0 to 1 using a modified fourth-order integral scheme [41] and the spectral integral method as discussed in the Appendix, respectively. The integrated values are denoted by U_h^{CN} and U_h^{SDC} . The exact integral of u_h^e along s from 0 to 1 can be obtained as U_h^e . The error is defined as

$$e^M = \|U_h^e - U_h^M\|_{\Omega_h},$$

where $M \in \{CN, SDC\}$. As Tab.3 presents, one can find that e^{SDC} achieves the error level about 4×10^{-6} only requiring 8 contour discretized nodes, while e^{CN} requiring 256 nodes. The error value of SDC method can only be reduced to about 4×10^{-6} due to the limitation of spatial discretization precision.

Table 3: The time integral error between the 4-order integral scheme and the spectral integral method

N_s	e^{CN}	e^{SDC}
4	4.2343e-03	2.4219e-04
8	1.0728e-03	4.4032e-06
16	2.6970e-04	4.0527e-06
32	6.7675e-05	4.0519e-06
64	1.7401e-05	4.0520e-06
128	5.8778e-06	4.0520e-06
256	4.1963e-06	4.0520e-06

4.1.2. Efficiency of SCFT calculations

To further demonstrate the performance of our proposed approach, we apply the numerical schemes to SCFT calculations. To compare results, we need a metric for accuracy that can be readily compared across different calculations. We use the value of single chain partition function Q as the solver's accuracy metric. Since it integrates the result of propagator solution, it is a measure of the entire solution. As a basis for comparison, we use a square with an edge length of $12R_g$ as the computational domain. The volume fraction of A is $f = 0.2$, and the interaction parameter $\chi N = 25$. The computation is carried out using a quadrilateral mesh (see Fig. 6 (a)). Correspondingly, the convergent morphology is a cylindrical structure, as shown in Fig. 6 (b).

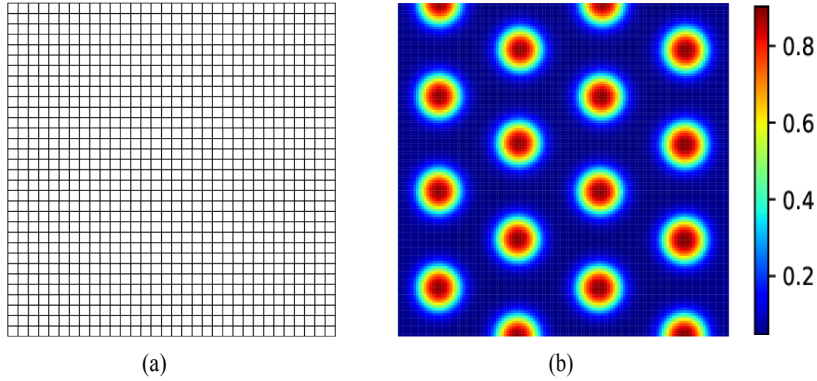


Figure 6: Cylindrical phase (b) calculated by VEM with uniform grid (a) when $\chi N = 25$, $f = 0.2$. Red colors correspond to large A-segment fractions.

First, we look at the contour discretization schemes. The goal is to have the fewest number of contour points necessary for a desired accuracy. The quadratic VEM with 32400 nodes is used to guarantee enough spatial discretization accuracy. Q_{ref} in Fig. 7(a) is numerically obtained by the SDC scheme with 160 contour points. Fig. 7(a) shows the convergent information of Q for the CN and SDC schemes, as discussed above. The SDC method converges faster than the CN scheme to a prescribed precision.

Second, we observe the numerical behavior of linear and quadratic VEMs in the SCFT simulation. From the above numerical tests (see Fig. 7(a)), one can see that using the SDC scheme with 160 discretization points can guarantee enough accuracy in the contour direction. So in the following computations, we use a high-precision numerical Q_{ref} as the exact value, which is obtained by the quadratic VEM with 32400 nodes and SDC scheme with 160 points. Fig. 7 (b) shows the Q values with different spatial discretization points of linear and quadratic VEMs. It is easy to see that the quadratic VEM is more accurate than the linear VEM as theory predicts. Therefore, in the following calculations, we always adopt the quadratic VEM and the SDC scheme.

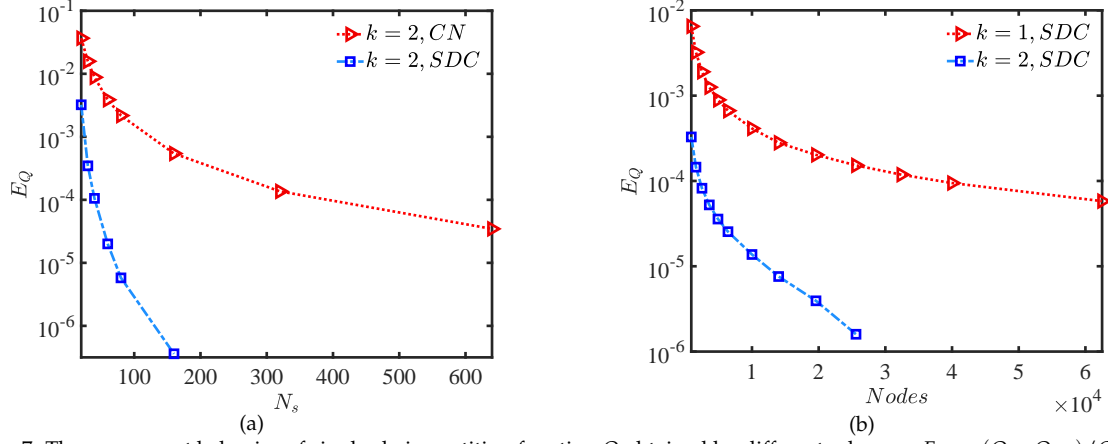


Figure 7: The convergent behavior of single chain partition function Q obtained by different schemes. $E_Q = (Q - Q_{ref})/Q_{ref}$ is the relative error. Q_{ref} is the numerically exact solution. (See text for the details about Q_{ref}). (a) shows Q obtained by the CN and SDC schemes as the contour points N_s increase. Quadratic VEM with 32400 nodes is employed to discretize the spatial variable. (b) presents Q computed by the linear and quadratic VEMs with an increase of spatial discretization points. SDC scheme with 160 points is used to discretize the contour variable.

4.1.3. General domains with general polygonal mesh

One advantage of VEM can use the arbitrary approximate geometry domain with general polygonal meshes. Fig. 8 presents these results on five different two-dimensional domains divided by quadrilateral and polygonal elements, respectively. The same convergent structure and almost the same Hamiltonian value can be obtained for these two kinds of meshes, as shown in Fig. 8 and Tab. 4.

Table 4: The number of nodes of different meshes used in SCFT calculations for five different domains as shown in Fig. 8 and corresponding converged Hamiltonian values.

Domain	Mesh	Nodes	Hamiltonian	
			(c)	(d)
Fig. 8 (1)	(a)	13041	-2.3742	-1.7388
	(b)	22560	-2.3754	-1.7398
Fig. 8 (2)	(a)	10720	-2.3720	-1.7440
	(b)	20273	-2.3765	-1.7382
Fig. 8 (3)	(a)	7014	-3.1410	-0.1874
	(b)	6510	-3.1409	-0.1873
Fig. 8 (4)	(a)	30182	-3.1440	-0.1900
	(b)	34587	-3.1448	-0.1901
Fig. 8 (5)	(a)	7601	-2.3670	-1.6797
	(b)	13824	-2.3718	-1.6883

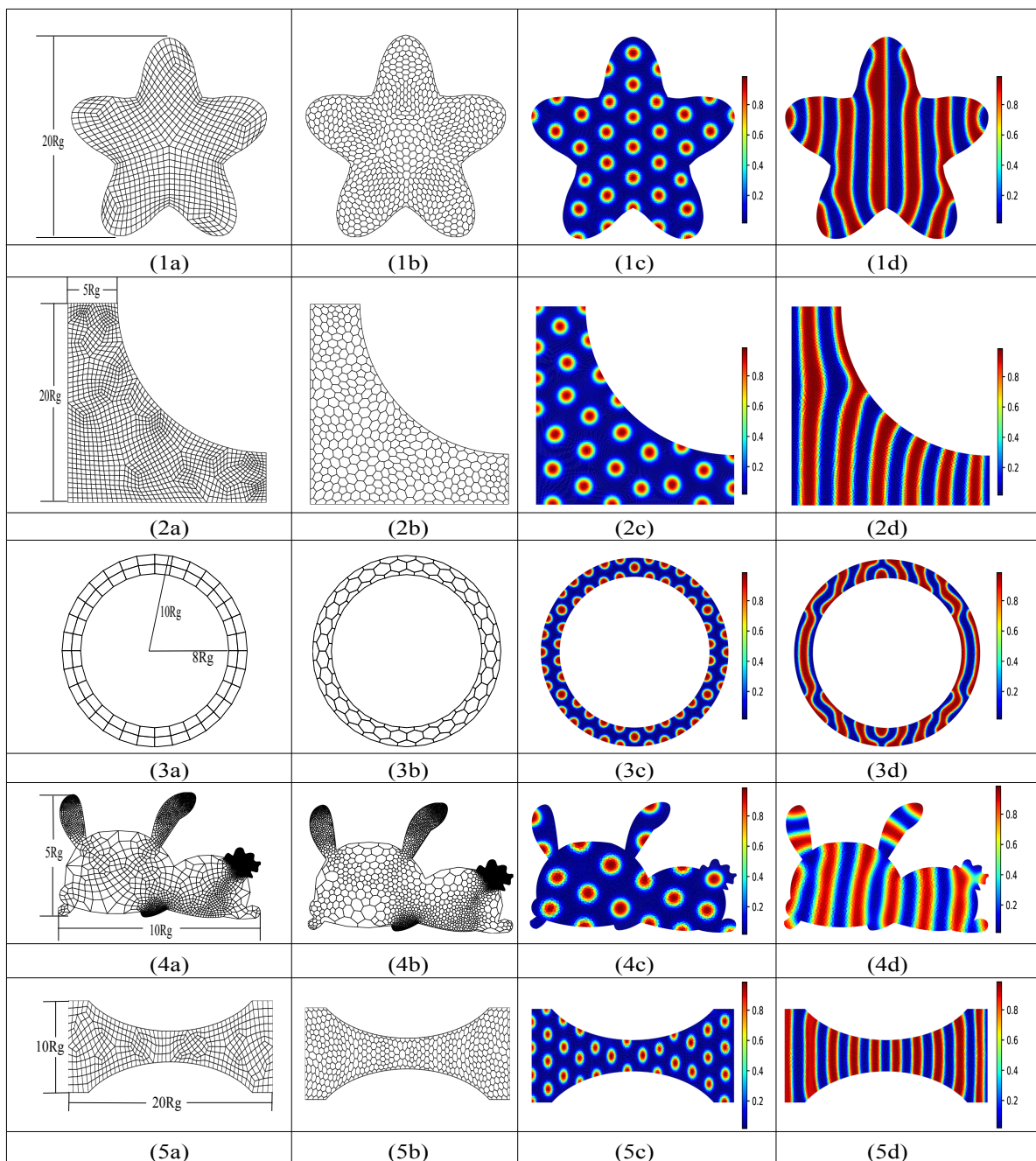


Figure 8: The self-assembled patterns in general domains through SCFT simulation, including (1). Flower shaped plane; (2). Curved-L shaped plane; (3). Ring domain; (4). Rabbit-shaped plane; and (5). Dumbbell plane. Red colors correspond to A-segment fractions. The first and second columns present the schematic mesh of quadrangular and polygonal meshes, respectively. The simulating diblock copolymer systems contain (1c) $[\chi N, f] = [25, 0.2]$, (1d) $[\chi N, f] = [15, 0.5]$, (2c) $[\chi N, f] = [25, 0.2]$, (2d) $[\chi N, f] = [15, 0.5]$, (3c) $[\chi N, f] = [30, 0.2]$, (3d) $[\chi N, f] = [14, 0.5]$, (4c) $[\chi N, f] = [30, 0.3]$, (4d) $[\chi N, f] = [14, 0.5]$, (5c) $[\chi N, f] = [25, 0.2]$, and (5d) $[\chi N, f] = [15, 0.5]$. The number of nodes of the mesh and converged Hamiltonian values can be found in Tab. 4.

4.2. VEM with adaptive mesh

In this subsection, we will demonstrate the efficiency of adaptive VEM from three parts: 1) the less computational cost to obtain prescribed accuracy compared with uniform mesh; 2) the application to strong segregation systems; 3) general domains with adaptive polygonal mesh. As discussed in Sec. 4.1.1, the quadratic VEM is more accurate than the linear one. Therefore, only quadratic VEM is used in the adaptive process. Meanwhile, the SDC scheme is chosen to discretize the contour variable with 100 points.

4.2.1. Efficiency

First, we take $\chi N = 25$ and $f = 0.2$ as an example to demonstrate the efficiency of adaptive VEM. The computational domain is a square with an edge length of $12R_g$. The square domain's uniform mesh with 1089 nodes is used to model the system at the start stage. Then adaptive VEM is launched when the iteration reaches the maximum step 500 or the reference value of the estimator $\eta_{ref} < 0.1$, where

$$\eta_{ref} = \sigma(\eta_E) / (\max(\eta_E) - \min(\eta_E)).$$

$\sigma(\eta_E)$ is the standard deviation of η_E , estimator η_E see Eqn. (10)). The adaptive process will be terminated when the successive Hamiltonian difference is smaller than 1.0×10^{-6} . Fig. 9 (a) gives the final adaptive mesh which includes 6684 nodes. Fig. 9 (b) shows the convergent tendency of Hamiltonian H of the adaptive process. The finally converged morphology has been shown in Fig. 6 (b). It can be seen that the Hamiltonian value efficiently converges by the cascadic adaptive method and refined meshes concentrate on the shape interface.

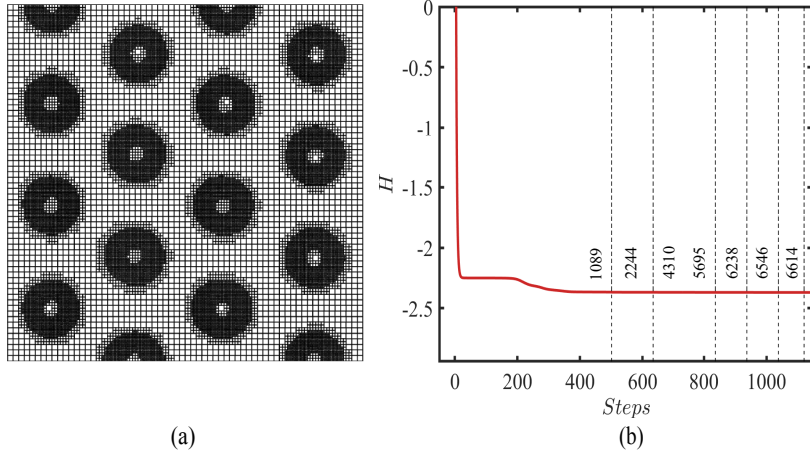


Figure 9: (a) The converged adaptive mesh. (b) The numerical behavior of Hamiltonian H . The numbers between two dotted lines represent the number of spatial nodes in the adaptive process.

We also compared the simulation results of VEM with adaptive and uniform mesh. Fig. 10 shows the numerical behaviors of single chain partition function Q and Hamiltonian H as the nodes increase. Tab. 5 gives the corresponding converged values of Q and H . From these results, one can find that the uniform mesh's results indeed gradually converge to that of adaptive VEM. However, there exists a small gap between the results of the two methods. The reason is that the adaptive VEM puts more meshes on the sharp interface and obtained a relatively accurate solution. The minimum element size of the adaptive mesh in the above calculation is $h_{min} = 0.0469R_g$. While the uniform mesh method with the same element size h_{min} requires about 65000 nodes, which is about ten times the adaptive approach.

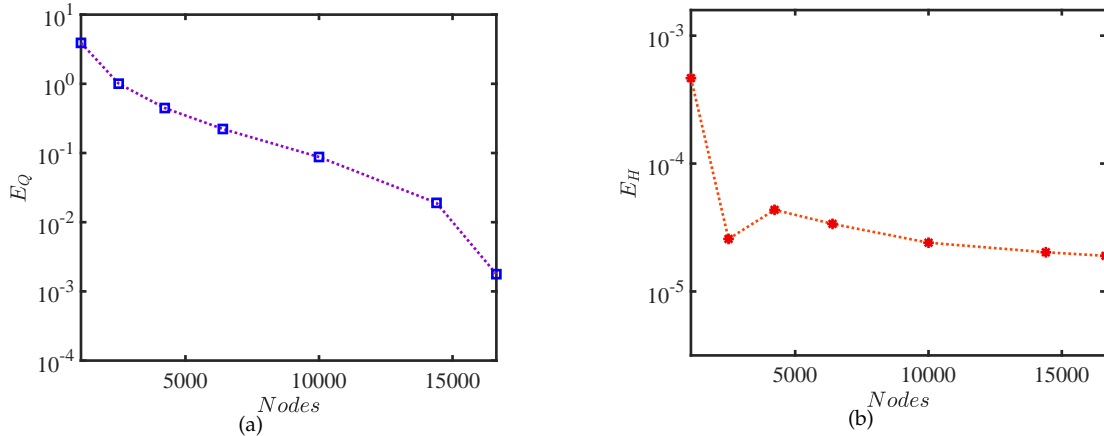


Figure 10: The convergence results of VEM with adaptive and uniform mesh when $\chi N = 25, f = 0.2$. The differences of (a) single partition function Q , $E_Q = (Q - Q_{adap}) / Q_{adap}$ and of (b) Hamiltonian value H , $E_H = (H - H_{adap}) / H_{adap}$. Q and H are obtained with uniform mesh, while Q_{adap} and H_{adap} are calculated with the adaptive approach.

Table 5: The convergence values of Q and H obtained by VEM with adaptive and uniform meshes.

Mesh	Nodes	Q	H
Adaptive	6684	4.2295e+02	-2.369403
Uniform	16641	4.2373e+02	-2.369448

4.2.2. Strong segregation systems

Next, we apply the adaptive VEM to simulate strong segregation systems, i.e., large interaction parameter χN , also in the square domain with an edge length of $12R_g$. For the strong segregation case, the interface thickness becomes narrower. Therefore the adaptive method is more suitable than the uniform mesh approach to catch these narrower interfaces. When simulating the strong segregation system, the initial values are obtained by the relatively weak segregation system's converged results. Tab. 6 presents the numerical results of χN from 25 to 60 and $f = 0.2$. From these results, one can find the advantages of the adaptive VEM as χN increases, including a mild increase of mesh nodes and fewer iteration steps.

Table 6: Numerical results by the adaptive VEM for strong segregation systems.

χN	Step	Nodes	H
25	1146	6684	-2.369403
30	78	9037	-3.149607
35	89	13443	-4.020791
40	74	17649	-4.946249
45	75	19741	-5.907039
50	75	20480	-6.892386
55	73	20641	-7.895548
60	61	20690	-8.911902

Finally, we apply the adaptive VEM to the strong segregation systems on more complicated domains, including two kinds of structures, spotted phases when $f = 0.2$ and lamellar phases when $f = 0.5$. Fig. 11 presents the adaptive meshes and converged morphologies. The corresponding nodes of uniform mesh are estimated by the minimum mesh size of the adaptive mesh. A comparison demonstrates that the adaptive method can greatly reduce the number of nodes as shown in Tab. 7.

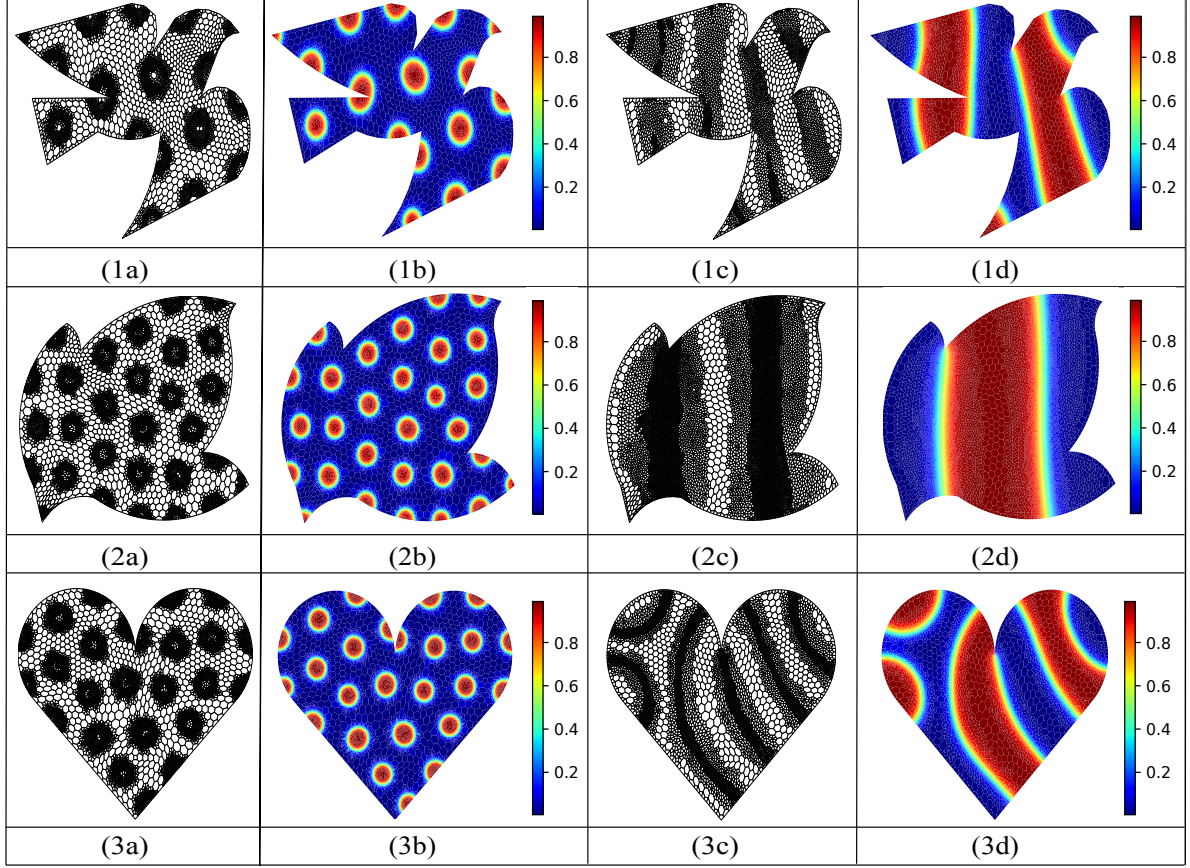


Figure 11: The self-assembled patterns of strong segregation systems obtained by the adaptive VEM, (a)(c) adaptive meshes, (b) spotted phases, (d) lamellar phases. The model parameters are (1b) $[\chi N, f] = [35, 0.2]$, (1d) $[\chi N, f] = [30, 0.5]$, (2b) $[\chi N, f] = [40, 0.2]$, and (2d) $[\chi N, f] = [40, 0.5]$. (3b) $[\chi N, f] = [40, 0.2]$, and (3d) $[\chi N, f] = [30, 0.5]$. Red colors correspond to large A-segment fractions.

Table 7: The corresponding data on three different planes as shown in Fig. 11. $Node_{adap}$ and h_{min} are the number of nodes and minimum grid size of the adaptive mesh, respectively. $Node_{uni}$ is the number of nodes of the uniform mesh with the same cell size estimated by h_{min} . $C_{save} = 1 - Node_{adap}/Node_{uni}$.

Mesh	h_{min}	$Node_{adap}$	$Node_{uni}$	$C_{save}(\%)$
Fig. 11(1)(a)	3.54e-02	8154	12956	37.1%
Fig. 11(1)(c)	1.17e-02	7591	26727	71.6%
Fig. 11(2)(a)	2.98e-02	19118	30169	36.6%
Fig. 11(2)(c)	2.12e-03	24138	116533	79.3%
Fig. 11(3)(a)	3.04e-02	14914	27729	46.2%
Fig. 11(3)(c)	1.33e-02	8399	25763	67.4%

5. Conclusion

In this paper, we propose an efficient numerical method to solve the polymer SCFT model on arbitrary domains based on the VEM. We have developed an adaptive method equipped with a new *Log* marking strategy that can make full use of the information of numerical results and save the SCFT iterations significantly. Using the halfedge data structure, we can apply an adaptive method to refine and coarsen arbitrary polygonal grids. The SDC method is also used to discretize the contour variable. The resulting method can obtain a high-accuracy numerical solution with fewer spatial and contour nodes. Numerical results demonstrate that the adaptive VEM even saves the computational amount up to 79.3% in solving a strong segregation lamellar system compared with the uniform mesh method. In this work, we have applied our algorithms to two-dimensional SCFT calculations. In future work, we aim to develop the adaptive VEM method to investigate three-dimensional SCFT problems.

Appendix: Spectral integral method along the contour variable s

In this Appendix, we discuss the Chebyshev-node interpolatory quadrature method [13] to integrate the residual error $\gamma^{[0]}(s)$ of Eqn. (12) for the contour variable s , which has spectral accuracy for smooth integrand [42]. The proposed scheme can also be applied to evaluating the density operators (3) and (4). These problems can be summarized to the following integral

$$\int_a^b g(s) ds,$$

where the integrand $g(s)$ is a smooth function. After changing variables, the general integral becomes

$$\int_a^b g(s) ds = \frac{b-a}{2} \int_0^\pi g(-\cos \theta) \sin \theta d\theta,$$

where $\theta \in [0, \pi]$. The interpolate polynomial of g at Chebyshev node $\theta_j = j\pi/N_s, j = 0, 1, \dots, N_s$.

$$g(-\cos \theta_j) \approx \frac{a_0}{2} + \sum_{k=1}^{N_s-1} a_k \cos(k\theta_j) + \frac{1}{2} a_{N_s} \cos(N_s \theta_j),$$

where

$$a_k = \frac{1}{N_s} g(-\cos \theta_0) \cos(k\theta_0) + \frac{2}{N_s} \sum_{j=1}^{N_s-1} g(-\cos \theta_j) \cos(k\theta_j) + \frac{1}{N_s} g(-\cos \theta_{N_s}) \cos(k\theta_{N_s}),$$

$k = 0, \dots, N_s$. In practice, coefficients a_0, a_1, \dots, a_{N_s} are calculated by the fast discrete cosine transform.

$$\int_0^\pi g(-\cos \theta) \sin \theta d\theta = \frac{a_0}{2} \int_0^\pi \sin \theta d\theta + \sum_{k=1}^{N_s-1} a_k \int_0^\pi \cos k\theta \sin \theta d\theta + \frac{a_{N_s}}{2} \int_0^\pi \cos N_s \theta \sin \theta d\theta.$$

Due to $\cos k\theta \sin \theta = \frac{1}{2} [\sin(1+k)\theta + \sin(1-k)\theta]$, we have

$$\int_a^b g(s) ds = \frac{b-a}{2} \int_{-1}^1 g(t) dt \approx \begin{cases} \frac{b-a}{2} \left[a_0 + \sum_{\substack{k=2 \\ k \text{ even}}}^{N_s-2} \frac{2a_k}{1-k^2} + \frac{a_{N_s}}{1-N_s^2} \right], & N_s \text{ is even,} \\ \frac{b-a}{2} \left[a_0 + \sum_{\substack{k=2 \\ k \text{ even}}}^{N_s-1} \frac{2a_k}{1-k^2} \right], & N_s \text{ is odd.} \end{cases}$$

References

- [1] C. R. Stewart-Sloan and E. L. Thomas. Interplay of symmetries of block polymers and confining geometries. *Eur. Polym. J.* 47 (04) (2011) 630-646.
- [2] R. A. Segalman. Patterning with block copolymer thin films. *Mater. Sci. Eng., R.* 46 (06) (2005) 191-226.
- [3] Y. Wu, G. Cheng, K. Katsov, S. W. Sides, J. Wang, J. Tang, G. H. Fredrickson, M. Moskovits, and G. D. Stucky. Composite mesostructures by nano-confinement. *Nat. Mater.*, 3 (11) (2004) 816-822.
- [4] A.-C. Shi and B. Li. Self-assembly of diblock copolymers under confinement. *Soft Matter*, 9 (2013) 1398-1413.
- [5] H. L. Deng, Y. C. Qiang, T. T. Zhang, W. Li, T. Yang. Chiral selection of single helix formed by diblock copolymers confined in nanopores. *Nanoscale*. 8 (2016) 15961-15969.
- [6] H. Wang, B. Shentu, R. Faller. Molecular dynamics of different polymer blends containing poly(2,6-dimethyl-1,4-phenylene ether). *Phys. Chem. Chem. Phys.* 17 (06) (2015) 4714-4723.
- [7] V. Sethuraman, B.H. Nguyen, V. Ganesan. Coarse-graining in simulations of multicomponent polymer systems. *J. Chem. Phys.* 141 (2014) 244904.
- [8] G.H. Fredrickson. *The equilibrium theory of inhomogeneous polymers*. Oxford University Press: New York, (2006).
- [9] W. Xu, K. Jiang, P.W. Zhang, A.C. Shi. A strategy to explore stable and metastable ordered phases of block copolymers. *J. Phys. Chem. B* 117 (17) (2013) 5296-5305.
- [10] K. Jiang, Y.Q. Huang, P.W. Zhang. Spectral method for exploring patterns of diblock copolymers. *J. Comput. Phys.* 229 (20) (2010) 7796-7805.
- [11] K. Jiang, C. Wang, Y.Q. Huang, P.W. Zhang. Discovery of new metastable patterns in diblock copolymers. *Commun. Comput. Phys.* 14 (02) (2013) 443-460.

- [12] G. Ouaknin, N. Laachi, K. Delaney, G.H. Fredrickson. Self-consistent field theory simulations of polymers on arbitrary domains. *J. Comput. Phys.* 327 (2016) 168-185.
- [13] H.D. Ceniceros. Efficient order-adaptive methods for polymer self-consistent field theory. *J. Comput. Phys.* 386 (01) (2019) 9-21.
- [14] H.D. Ceniceros, G.H. Fredrickson. Numerical solution of polymer self-consistent field theory. *Multiscale Model. Simul.* 2 (03) (2004) 452-474.
- [15] R.B. Thompson, K.Ø. Rasmussen, T. Lookman. Improved convergence in block copolymer self-consistent field theory by anderson mixing. *J. Chem. Phys.* 120 (31) (2004) 31-34.
- [16] K. Jiang, W.Q. Xu, P.W. Zhang. Analytic structure of the SCFT energy functional of multicomponent block copolymers. *Commun. Comput. Phys.* 17 (05) (2015) 1360-1387.
- [17] M.W. Matsen, M. Schick. Stable and unstable phases of a diblock copolymer melt. *Phys. Rev. Lett.* 72 (16) (1994) 2660-2663.
- [18] K.Ø. Rasmussen, G. Kalosakas. Improved numerical algorithm for exploring block copolymer mesophases. *J. Phys.: Condens. Matter* 40 (16) (2002) 1777-1783.
- [19] E.W. Cochran, C.J. Garcia-Cervera, G.H. Fredrickson. Stability of the gyroid phase in diblock copolymers at strong segregation. *Macromolecules* 39 (07) (2006) 2449-2451.
- [20] D.M. Ackerman, K. Delaney, G.H. Fredrickson, B. Ganapathysubramanian. A finite element approach to self-consistent field theory calculations of multiblock polymers. *J. Comput. Phys.* 331 (2017) 280-296.
- [21] H.Y. Wei, M. Xu, W. Si, K. Jiang. A finite element method of the self-consistent field theory on general curved surfaces. *J. Comput. Phys.* 387 (15) (2019) 230-244.
- [22] P. Binev, W. Dahmen, R. DeVore. Adaptive finite element methods with convergence rates. *Numer. Math. (Heidelb)*, 97 (02) (2004) 219-268.
- [23] C. Carstensen, J. Hu. Hanging nodes in the unifying theory of a posteriori finite element error control. *J. Comput. Math.*, (2009) 215-236.
- [24] B. Ahmed, A. Alsaedi, F. Brezzi, L.D. Marini, A. Russo. Equivalent projectors for virtual element methods. *Comput. Math. Appl.*, 66 (03) (2013) 376-391.
- [25] L. Beirao da Veiga, F. Brezzi, L.D. Marini, A. Russo. The hitchhiker's guide to the virtual element method. *Math. Models Methods Appl. Sci.* 24 (08) (2014) 1541-1573.
- [26] L. Beirao da Veiga, F. Brezzi, A. Cangiani, L.D. Marini, G. Manzini, A. Russo. Basic principles of virtual elements methods. *Math. Models Methods Appl. Sci.* 23 (2013) 199-214.
- [27] P.F. Antonietti, L. Beirão da Veiga, D. Mora, M. Verani. A stream function formulation of the Stokes problem for the virtual element method. *SIAM J. Numer. Anal.* 52 (2014) 386-404.
- [28] J.K. Zhao, S.C. Chen, B. Zhang. The nonconforming virtual element method for plate bending problems. *Math. Models Methods Appl. Sci.* 26 (2016) 1671-1687.
- [29] L. Chen, H.Y. Wei, M. Wen. An interface-fitted mesh generator and virtual element methods for elliptic interface problems. *J. Comput. Phys.* 334 (2017) 327-348.
- [30] Y.Q. Huang, K. Jiang, N.Y. Yi. Some weighted averaging methods for gradient recovery. *Adv. Appl. Math. Mech.* 4 (02) (2012) 131-155.
- [31] H. Jarausch. On an adaptive grid refining technique for finite element approximations. *SIAM J. Sci. and Stat. Comput.*, 7(04) (1986) 1105-1120.
- [32] W. Dörfler. A convergent adaptive algorithm for poisson's equation. *SIAM J. Numer. Anal.*, 33(03) (1996) 1106-1124.
- [33] <http://www.danenglesson.com/images/portfolio/MoA/halfedge.pdf>
- [34] R. E. Bank, A. H. Sherman, and A. Weiser. Refinement algorithms and data structures for regular local mesh refinement, *Scientific computing (Montreal, Que., 1982)*, IMACS Trans. Sci. Comput., I, IMACS, New Brunswick, NJ, 1983, pp. 3-17.
- [35] M. C. Rivara, Mesh refinement processes based on the generalized bisection of simplices, *SIAM J. Numer. Anal.*, 21 (1984), pp. 604-613.
- [36] L. Chen and C-S. Zhang. A coarsening algorithm on adaptive grids by newest vertex bisection and its applications. *Journal of Computational Mathematics*, 28(6):767-789, 2010.
- [37] H.Y. Wei, Y.Q. Huang. FEALPy: finite element analysis library in Python. <https://github.com/weihuayi/fealpy>, Xiangtan University, 2017-2021.
- [38] A. Dutt, L. Greengard, V. Rokhlin. Spectral deferred correction methods for ordinary differential equations. *BIT Numer. Math.*, 40 (02) (2000) 241-266.
- [39] C.W. Clenshaw, A.R. Curtis. A method for numerical integration on an automatic computer. *Numer. Math. (Heidelb)*, 2 (01) (1960) 197-205.
- [40] U.M. Ascher, S.J. Ruuth, R.J. Spiteri. Implicit-explicit Runge-Kutta methods for time-dependent partial differential equations. *Appl. Numer. Math.*, 25 (1997) 151-167.
- [41] See the formula (4.1.14) on p. 160 in *Numerical recipes: the art of scientific computing*, 3rd edition, W.H. Press, A.S. Teukolsky, W.T. Vetterling, B.P. Flannery, Ed. Cambridge University Press, New York (2007).
- [42] L.N. Trefethen. Is Gauss quadrature better than Clenshaw-Curtis? *SIAM Review*, 50 (01) (2008) 67-87.